

Second-harmonic generation and x-ray diffraction studies of the pretransitional region and polar phase in relaxor $K_{(1-x)}Li_xTaO_3$

Hiroko Yokota* and Yoshiaki Uesu

*Department of Physics, Faculty of Science and Engineering, Waseda University, 3-4-1 Okubo, Shinjuku-ku, Tokyo 169-8555, Japan*Charlotte Malibert¹ and Jean-Michel Kiat^{1,2}¹*Structures, Propriétés, Modélisation des Solides, UMR 8580 au CNRS, Ecole Centrale Paris, Grande Voie des Vignes, 92295 Chatenay Malabry Cedex, France*²*Laboratoire Leon-Brillouin, CE Sacray, 91191 Gif-sur-Yvette Cedex, France*

(Received 10 October 2006; revised manuscript received 3 March 2007; published 29 May 2007)

Optical second-harmonic generation (SHG) observations and precise x-ray diffraction experiments have been performed on quantum paraelectrics $KTaO_3$ (KTO) and relaxors $K_{(1-x)}Li_xTaO_3$ with $x=3\%$ (KLT-3) and 7% (KLT-7). It is found in KLT-3 and KLT-7 that a pretransitional region exists between two characteristic temperatures T_B and $T_p (< T_B)$. The average symmetry of the region is tetragonal with a weak lattice deformation, but it is nonpolar on average. The temperature interval between T_B and T_p is consistent with the interval in which neutron diffuse scatterings have been previously reported. T_B is also found to align with the deviation temperature of the Curie-Weiss behavior of dielectric constant. These facts strongly suggest that polar nanoregions (PNRs) nucleate around T_B and grow toward T_p . Below T_p , a larger deformation and a field-induced SH intensity start to develop, while no significant SHG appears in the zero-field-cooling (ZFC) process because of macroscopic inversion symmetry of the polydomain structure. The field-cooling (FC) process breaks the macroscopic inversion symmetry and the temperature dependence of SH intensity in field heating after FC coincides well with that of the tetragonality determined by x-ray diffraction experiments. The Landau-Devonshire phenomenological approach suggests that the ferroelectric phase transition at T_p is of first order and that it approaches the second-order transition with a decrease in the Li concentration. A marked increase of neutron-diffraction intensities below T_p , together with the disappearance of SHG intensity in a ZFC run, indicates that PNRs are transformed to ferroelectric microdomains at T_p . The microdomains become macroscopic below T_p in the FC process. In the lower-temperature region, nonergodic behavior was observed: The ZFC state cannot approach the thermodynamically equilibrium state under the electric field within finite time.

DOI: [10.1103/PhysRevB.75.184113](https://doi.org/10.1103/PhysRevB.75.184113)

PACS number(s): 64.70.Kb, 42.65.Ky, 61.50.Ks, 61.72.Ww

I. INTRODUCTION

Quantum paraelectrics are dielectrics in which the condensation of a low-lying transverse-optical mode is prevented by the quantum fluctuation of atoms. As a result, the divergence of the dielectric constant indicating a ferroelectric phase transition does not occur down to 0 K, although the dielectric constant increases with decreasing temperature toward a high value of several thousands. In this sense, quantum paraelectrics are incipient ferroelectrics and a small addition of impurities or an application of external forces can induce ferroelectricity. In particular, with the substitution of Li ions in quantum paraelectric $KTaO_3$ (KTO) (henceforth, we use an abbreviation KLT- $x\%$ for $K_{(1-x)}Li_xTaO_3$), a dielectric peak appears at low temperatures and the peak temperature (T_m) increases with the Li concentration.¹ However, the polar state below T_m is not well understood. Some reports insist that it is a long-range ferroelectric phase,^{2,3} and others explain it with the dipole glass picture.^{1,4} An x-ray diffraction study reveals that a tetragonal strain appears above $x=5\%$, which indicates that the long-range order develops with higher Li concentrations.⁵ On the other hand, Toulouse *et al.* pointed out that KLT is a kind of relaxor based on dielectric dispersion characteristics⁶ and neutron diffuse scattering experiments.⁷ Recent observations using an optical second-harmonic generation (SHG) microscope also support

the relaxor nature of KLT-3 because of the marked history dependence of SHG intensities⁸ which is similar to that of a prototype relaxor $Pb(Mg_{1/3}Nb_{2/3})O_3$ (PMN).^{9,10} To be a real relaxor, the following criteria should be satisfied: (1) the characteristic frequency dispersion obeys the Vogel-Fulcher (VF) law and (2) polar nanoregions (PNRs) appear in a temperature range above T_m . Additionally, the history dependence and the slow time evolution of the order parameter are significant indicators of relaxors. Although some of these characteristics have been reported for specific Li concentrations, the characteristic temperature (Burns temperature T_B) where PNRs appear has not been explicitly discussed yet. For this purpose, two kinds of measurements are necessary, one being sensitive to a lattice deformation and the other to a polar state. With this motivation, we investigate KLTs using the SHG microscope which is quite susceptible to polarization changes and x-ray diffraction which is sensitive to minute lattice deformations. In addition to these measurements, neutron-scattering experiments and dielectric measurements are performed on KLT-3 and KLT-7, and pure KTO as a reference crystal to prove the above-mentioned criteria.

II. EXPERIMENTAL CONDITIONS

A pure KTO single crystal is grown by the top-seeded crystal growth method. KLT-3 and KLT-7 single crystals are

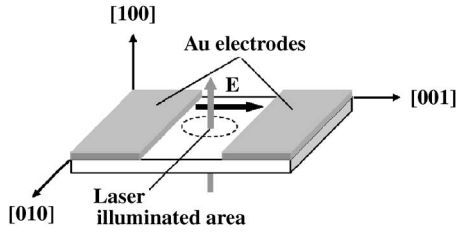


FIG. 1. Sample orientation and directions of the electric field and laser beam.

grown by the self-flux method with Ta_2O_5 , Li_2CO_3 , and an excess of K_2CO_3 as a flux.¹¹ The exact Li concentration x is determined by the empirical relation between x and the transition temperature T_p .¹² T_p is defined by the disappearance temperature of SH intensity in zero-field heating (ZFH) after the field-cooling (FC) process. See Ref. 8 for more details.

SHG images are obtained by the SHG microscope which provides the distribution of the SH intensities in a specimen.^{13,14} We use a Q -switched Nd^{3+} :YAG (yttrium aluminum garnet) laser with a wavelength of 1064 nm, a repetition frequency of 20 Hz, and an energy per pulse of 15 mJ as a fundamental light source. The polarization direction can be changed by a half-wave plate. SH waves with a 532 nm wavelength generated in a specimen are detected by an image-intensified charge coupled device camera that is located behind an analyzer and a band-pass filter. The typical exposure time is about 10 s and is changed from 5 to 15 s depending on the magnitude of the SH intensity. A specimen is put in a liquid-He cryostat (CF2101, Oxford Instruments) for microscopy. The temperature stability of a specimen during the exposure time is about 0.5 K. Temperature rise by laser illumination is within 0.5 K, which is consistent with the calculated value with the specific heat¹⁵ and thermal conductivity¹⁶ of KLT.

(100) plate specimens are cut from single crystals and optically finished. Au electrodes are evaporated on a (100) top surface and an electric field is applied along the [001] direction in the sample plane.¹⁷ The incident laser beam of 3 mm diameter is positioned between two electrodes so as to avoid a photoconductivity observed at low temperature. The sample orientation and directions of the electric field and laser beam are illustrated in Fig. 1.

X-ray diffraction measurements are performed on a highly accurate two-axis diffractometer with a Bragg-Brentano geometry using $\text{Cu } K\beta$ wavelength ($\lambda=0.139\ 223$ nm) from an 18 kW rotating anode generator, equipped with a liquid-He cryostat. The lattice constants are determined from profiles of (400) reflections using pseudo-Voigt analysis. We use (001) plate specimens with an area of 5×3 mm² and a thickness of 0.65 mm.

Neutron-diffraction experiments are performed using a triple-axis spectrometer T1-1HQ installed in JRR-3M in Japan Atomic Energy Agency with the incident energy of neutron beams of 13.60 meV ($\lambda=0.2459$ nm). The horizontal collimator sequence is a monochromator-20'-sample-40'-detector. Sample dimensions are $6.0 \times 5.5 \times 3$ mm³ for KLT-3 and $4.5 \times 4.5 \times 3$ mm³ for KLT-7.

The complex impedances Z' (real part) and Z'' (imaginary part) of the sample are measured by a Solartron SI-1255B

frequency response analyzer with SI-1296 dielectric interface. The complex dielectric constants ϵ' (real part) and ϵ'' (imaginary part) are calculated from the impedance and sample dimensions. Measurements of temperature dependence are performed from 20 to 290 K with a frequency range from 10 Hz to 1 MHz with an ac amplitude of 1 V_{rms}.

III. EXPERIMENTAL RESULTS AND ANALYSES

A. SHG microscopic observations

Temperature dependences of SH intensity distributions of pure KTO, KLT-3, and KLT-7 are observed using the SHG microscope. The observations are carried out in different paths in the E - T diagram, i.e., zero-field-cooling (ZFC), ZFH after ZFC (ZFH/ZFC), FC, field heating after FC (FH/FC), and ZFH after FC (ZFH/FC) processes. The electric field in FC and FH processes is fixed to be 80 V/mm. ZFC and ZFH/ZFC processes give no significant SHG for all specimens because of macroscopic inversion symmetry of polydomain structure. A FC process breaks the macroscopic inversion symmetry and produces strong SHG in KLT-3 and KLT-7. ZFH/FC and FH/FC show almost the same results within experimental error. Figure 2 shows temperature dependences of SH intensity averaged over a homogeneous area (0.05 mm²) in SHG images in FC and FH/FC processes. SH intensities of pure KTO at 22 K are almost 100 times weaker than those of the other two specimens. Moreover, the latter exhibits significant SHG signals that increase with Li concentration. As shown in the SHG images, distributions of SH intensity are inhomogeneous due mainly to the fact that a small portion of the sample is still in a polydomain state under the electric field. A stronger electric field (≥ 100 V/mm) makes the domain state single, but we did not apply this electric field because of the high photoconductivity observed below 70 K.

Weak SH intensities of pure KTO are observed only below 30 K, while much stronger SH intensities of KLT-3 and KLT-7 appear below 50 and 90 K, respectively. This phenomenon indicates that a macroscopic polar phase appears at the temperatures (T_p) under the electric field. Thus, T_p is a ferroelectric phase-transition temperature. Noticeable thermal hysteresis of about 7 K is observed in KLT-7 but not in KLT-3 within temperature fluctuation. Contrary to the FH/FC process, FH/ZFC shows quite different features, as shown in Fig. 3 for KLT-7. Weak SH intensities at low temperatures start to increase with raising temperature, showing a maximum that decreases and vanishes at 90 K. A similar phenomenon is also observed in KLT-3.⁸ This fact indicates that the FH/ZFC process is not the equilibrium but rather it is a non-equilibrium state and depends on the heating speed. It is possible that FH/FC and FH/ZFC will coincide with infinite time. In fact, we have recently found extremely slow kinetics of SH intensities of KLT-3 toward the FH/FC values under the electric field at a fixed temperature below T_p .¹⁸

B. X-ray diffraction studies

Absolute values of lattice constants of pure KTO, KLT-3, and KLT-7 at room temperature are determined using several

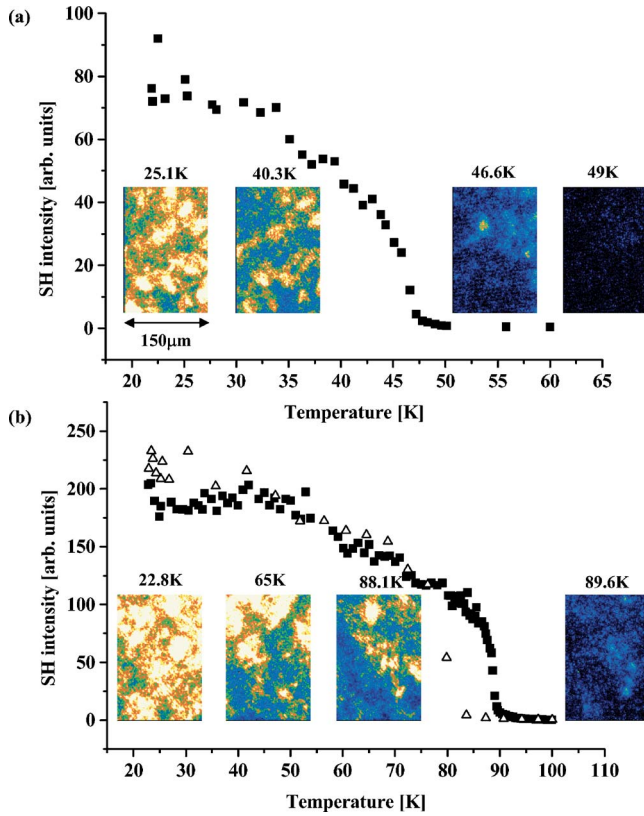


FIG. 2. (Color online) Temperature dependence of SH intensities of (a) KLT-3 and (b) KLT-7 in the FH/ZFC process. SHG images taken at some temperatures are also shown. In (b), the open triangles indicate the result of the FC process, and the solid squares indicate that of the FH/FC. SHG images do not represent in real color but virtual for getting high visibility. The brightness is proportional to the SHG intensity but cannot be compared with different specimens because the optimum treatment of brightness is made in each specimen by an imaging program.

($h00$) reflections. The result is shown in Fig. 4 with the previously reported values¹⁹ for comparison. A small difference of 0.01% is observed in the absolute values, but the relative variations with the Li concentration are consistent with the

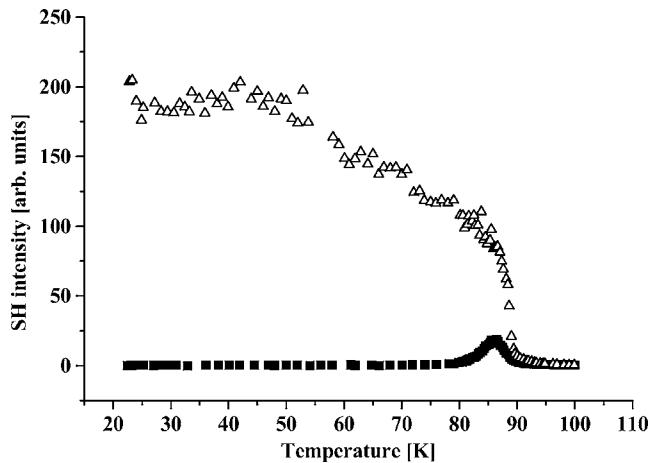


FIG. 3. Temperature dependences of SH intensities of KLT-7 in the FH/ZFC (solid squares) and FH/FC processes (open triangles).

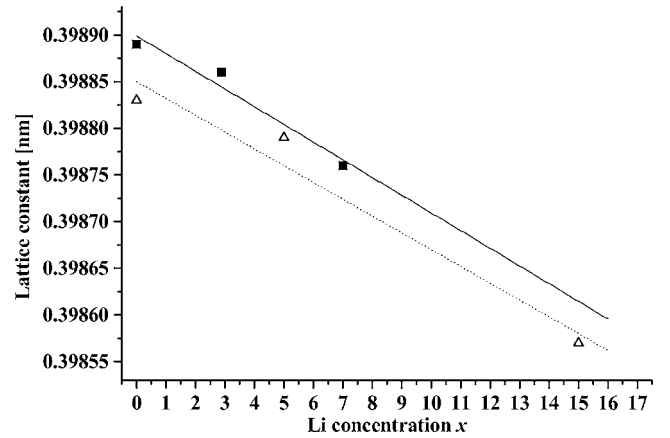


FIG. 4. Dependence of the absolute lattice constant a of KLT- x on Li concentration x . The solid squares indicate the present results and the open triangles indicate those reported in Ref. 19.

reported values. The lattice constant $a(x)$ of KLT- x decreases almost linearly with x . Assuming that the lattice contraction is caused by an effective ionic radius $R_0(\text{Li}^+)$ of Li^+ , we obtain the following relation:

$$a(x) = a(\text{pure KTO}) \left[1 + \frac{\Delta R}{R(\text{K}^+)} x \right], \quad (1)$$

where $R(\text{K}^+)$ is an ionic radius of K^+ and

$$\Delta R = R_0(\text{Li}^+) - R(\text{K}^+). \quad (2)$$

From the experiment, we obtain

$$\frac{\Delta R}{R(\text{K}^+)} \sim -0.0048. \quad (3)$$

When we take into account the fact that Li ions occupy off-center positions with deviations δ from the ideal A sites, the effective radius of Li ion is expressed as $\delta + [R(\text{Li}^+)/2]$. From the present experiment and using the ionic radii of K^+ (0.164 nm for the coordination number of 12) and Li^+ (0.059–0.092 nm depending on the coordination number),²⁰ δ is estimated to be 0.117–0.134 nm, which coincides well with the value of 0.12 nm obtained by the NMR measurement.¹³ This implies that the deviation δ is equally oriented along the $\langle 100 \rangle$ direction in KTaO_3 rigid lattices of KLT-3 and KLT-7.

The temperature dependences of lattice constants of KTO, KLT-3, and KLT-7 are plotted in Fig. 5. These are measured in the ZFC process. We also make the measurements in the FC and FH/FC processes. However, as the remarkable photoconductivity rises with x-ray illumination below 70 K, an efficacious electric field cannot be applied.

As shown in Fig. 5, the temperature dependence of the lattice constant of pure KTO is well fitted by the Debye formula

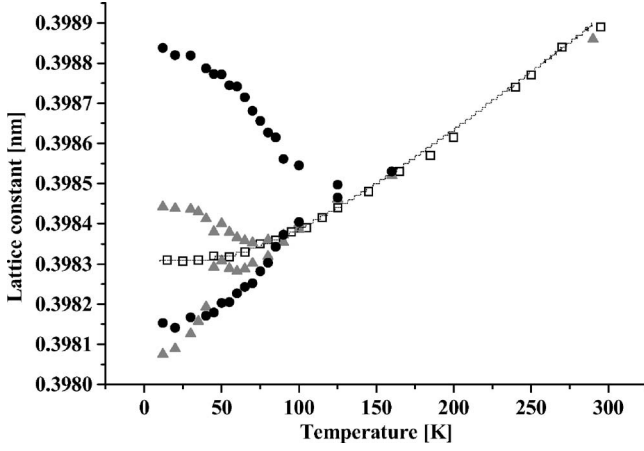


FIG. 5. Temperature dependences of lattice constants of KTO (open squares), KLT-3 (gray triangles), and KLT-7 (solid circles). The Debye fitting for KTO is plotted with the dotted line.

$$a = a_0 + A9RT \left(\frac{T}{\theta_D} \right)^3 \int_0^{\theta_D/T} \frac{t^3}{e^t - 1} dt, \quad (4)$$

with parameters $a_0 = 0.398\,317(3)$ nm, $A = 10^{-7}$ nm mol/J, and $\theta_D = 312(16)$ K.

In KLT-3 and KLT-7, the splitting of the (400) spectrum as a result of tetragonal deformation is observed at low temperatures and becomes significant with an increase in the Li concentration. Although the result agrees qualitatively with the reported values,^{5,8} a substantial difference exists: The present experiment using the high-precision diffractometer reveals that tetragonal deformation develops in two steps. With decreasing temperature, a small deformation appears at T_B (~ 90 K for KLT-3 and ~ 140 K for KLT-7) prior to a larger deformation at T_p (50 K for KLT-3 and 90 K for KLT-7).

To make this fact clearer, the tetragonality t defined by $2(c-a)/(c+a)$ is plotted together with SH intensities in the FH/FC process in Fig. 6. It should be noted that the electric-field-induced SHG appears at T_p and not at T_B . This fact

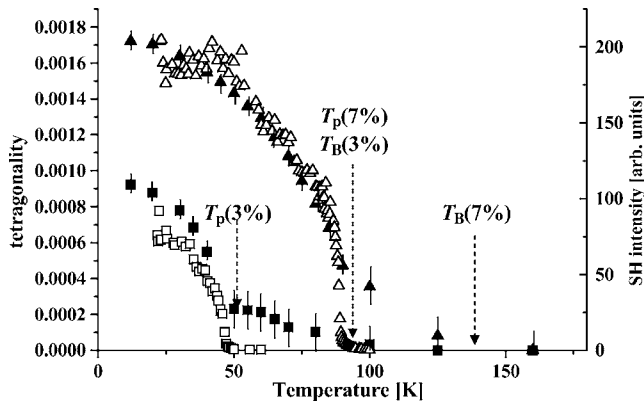


FIG. 6. Temperature dependences of tetragonality of KLT-3 (solid squares) and KLT-7 (solid triangles) in the ZFC process and SHG intensities of KLT-3 (open squares) and KLT-7 (open triangles) in the FH/FC process.

strongly suggests that a pretransitional region exists between T_B and T_p . The region is accompanied with a small tetragonal deformation that is nonpolar on average because of a lack of SHG. Below T_p , the temperature dependence of tetragonality coincides well with that of SH intensity under an electric field.

The SH intensity $I^{(2\omega)}$ is expressed by the following expression:²¹

$$I^{(2\omega)} = 2\omega^2 \left(\frac{\mu_0}{\varepsilon_0} \right)^{3/2} \frac{1}{n^{(2\omega)} [n^{(\omega)}]^2} (\varepsilon_0 d)^2 [I^{(\omega)}]^2 \frac{4 \sin^2 \left(\frac{1}{2} \Delta k L \right)}{(\Delta k)^2}. \quad (5)$$

Here, ω indicates the frequency of the fundamental wave, $n^{(\omega)}$ and $n^{(2\omega)}$ indicate the refractive index of the fundamental and SH waves, respectively, $I^{(\omega)}$ represents the intensity of the fundamental wave, Δk is the misfit parameter of wave numbers between the fundamental and SH waves, and L represents the specimen thickness. The constant d is a SHG tensor component, and in the present experiment, it is d_{33} in the Voigt notation with the polarization directions of the fundamental and SH waves parallel to the [001] direction. Since the product of d_{33} and P_3 is invariant on the group-theoretical consideration,²² d_{33} changes linearly with P . Therefore, $I^{(2\omega)}$ is proportional to P^2 . Through the electrostrictive effect, the tetragonality t is also proportional to P^2 . This explains the coincidence between $I^{(2\omega)}$ and t observed below T_p .

C. Phenomenological analyses of experimental results

We apply the Landau-Devonshire phenomenological theory to the temperature dependence of SH intensities in FH/FC processes. The free energy expanded up to the sixth power of P is expressed as²³

$$F = \frac{1}{2} \alpha (T - T_0) P^2 + \frac{1}{4} \beta P^4 + \frac{1}{6} \gamma P^6. \quad (6)$$

The equilibrium and stability conditions give²⁴

$$P^2 = \frac{-\beta + \sqrt{\beta^2 - 4\alpha\gamma(T - T_0)}}{2\gamma}. \quad (7)$$

The experimental results of SHG are fitted using Eq. (7) and are shown in Fig. 7. In the figure, the experimental result of KLT-1.7 under the same magnitude of E is also shown. The coefficients in the free energy determined by the fittings are tabulated in Table I, where the magnitudes of α of KLT-3 and KLT-7 are fixed at the values estimated from the dielectric constants in the higher-temperature region. The calculated curves agree well with the experimental ones. It should be noted that the order of phase transition of KLT-1.7 is the second since $\beta > 0$ and first for KLT-3 and KLT-7 ($\beta < 0$) and that the first-order nature becomes stronger with an increase in the Li concentration. In fact, the maximum thermal hysteresis width $\Delta T_{\text{hys}} = \beta^2 / 4\alpha\gamma$ of KLT-7 calculated with the free-energy coefficients is 3 K, while a much smaller value of $\Delta T_{\text{hys}} (= 0.014$ K) is obtained for KLT-3. The result

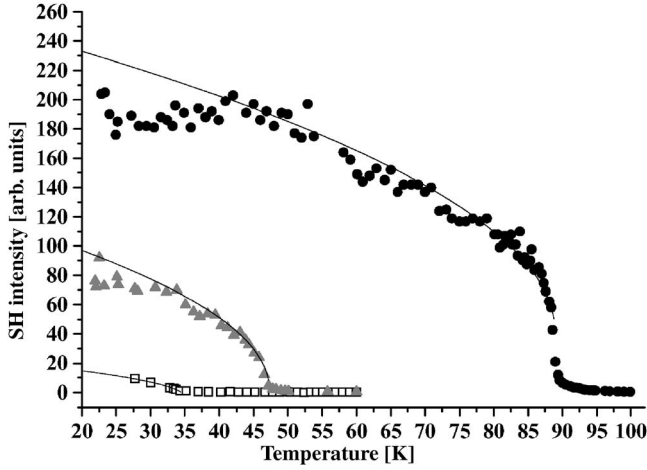


FIG. 7. Temperature dependences of SH intensities KLT-1.7 (open squares), KLT-3 (gray triangles), and KLT-7 (solid circles) in the FH/FC process. The solid lines are the fitting curves using the Landau-Devonshire theory.

is also supported by the experimental fact that a clear thermal hysteresis is found in KTL-7 but not in KLT-1.7 and KLT-3.

D. Dielectric measurements

Temperature dependence of dielectric constants of pure KTO and KTO doped with different Li concentrations has already been reported.^{6,25–27} The essential feature of our results is the same as those reported. Here, we show our results for KLT-3 and KLT-7 to clarify the behaviors at both characteristic temperatures T_B and T_p and to compare the parameters determined using the VF law with those of PMN.²⁸

Figure 8 shows the result of KLT-3 in ZFH/ZFC, with the real part ϵ' in (a) and the imaginary ϵ'' in (b). In addition to a pronounced peak with the characteristic frequency dispersion, small peaks are observed around T_B ($=90$ K), in particular, in the imaginary part. As shown in an inset figure of Fig. 8(b), T_m shifts to a higher side with increasing frequency. This kind of dispersion is characteristic in heterogeneous dielectrics and could be related to the appearance of PNRs.

Figure 9 shows the result of KLT-7 in the ZFH/ZFC process, where (a) indicates ϵ' and (b) indicates ϵ'' . The dispersion around T_B is not clearly observed in comparison with KLT-3, probably because the strong first-order nature at T_p hides small changes around T_B . Instead, the inverse of the dielectric constant is plotted against temperature and shown in Fig. 9(a). It is pointed out in prototype relaxor PMN that the deviation temperature from the Curie-Weiss behavior is

TABLE I. Coefficients in the Landau-Devonshire theory.

Substance	T_0 (K)	α	β	γ
KLT-1.7	34.5	1.0×10^{-5}	3.20×10^{-1}	4.53×10^3
KLT-3	47.3	1.13×10^{-5}	-1.49×10^{-2}	3.44×10^2
KLT-7	85.9	1.16×10^{-5}	-1.76×10^{-1}	2.16×10^2

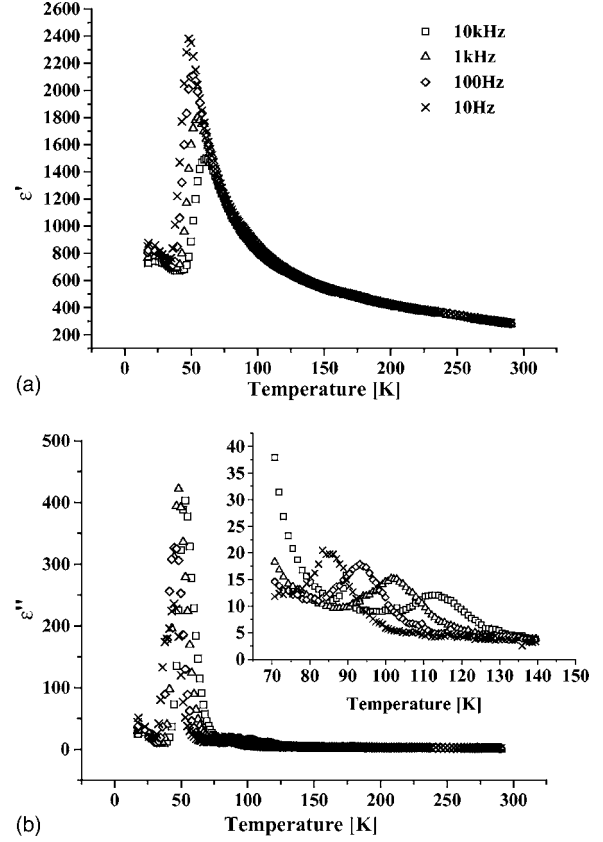


FIG. 8. Temperature dependences of (a) real part ϵ' and (b) imaginary part ϵ'' of the complex dielectric constant of KLT-3 in the ZFH/ZFC process as a parameter of frequency. The inset in (b) indicates the enlarged figure near T_B .

the Burns temperature at which PNRs appear.²⁹ The least-squares fitting of dielectric constant in the high-temperature region determines that the temperature is about 145 K, which is in accordance with T_B determined by the x-ray diffraction experiment.

At lower temperatures, a feature becomes visible: A sudden drop of ϵ' is observed at $T_p=90$ K. This phenomenon was also reported in KLT-3.5 in the lower-frequency region;⁶ however, a steep change in ϵ' is more clearly observed in the higher-frequency region. The reason for this difference is not clear at present. This shows that the ferroelectric phase transition takes place at T_p in some portions of the specimen. We shall discuss this more precisely in the next section.

Observed dielectric responses are analyzed with the VF law connecting the frequency f_m and the temperature T_m of the maximum ϵ' in a dipole or spin-glass system:

$$f_m = f_0 \exp[-E_a/k_B(T_m - T_{VF})], \quad (8)$$

where f_0 is the characteristic frequency, E_a is the activation energy, k_B is the Boltzmann factor, and T_{VF} is the freezing temperature below which dipoles cannot respond to the electric field. In KLT-7, two peaks are observed in ϵ' and the peak at higher temperature is used for the VF analysis. Table II shows the parameters of KTL-3 and KTL-7 determined by the present experiments and those of PMN.²⁹ The activation

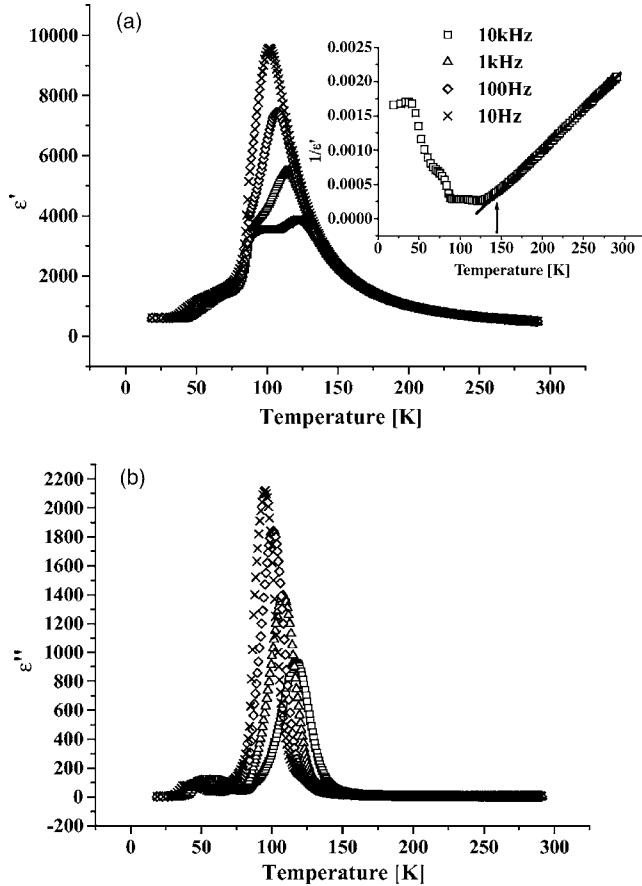


FIG. 9. Temperature dependences of (a) real part ϵ' and (b) imaginary part ϵ'' of the complex dielectric constant of KLT-7 in the ZFC/ZFC process as a parameter of frequency. The inset in (a) shows the inverse of dielectric constant at 10 kHz. The solid line indicates the least-squares fit in high-temperature region. The deviation temperature from the Curie-Weiss behavior is determined to be 145 K.

energy of KLT-7 is larger than that of KLT-3. This fact is related to the increase of the anisotropy energy with the Li concentration, since E_a is the product of an electrocrystalline anisotropy energy density and the volume of PNR.²⁸ On the other hand, no marked difference is found in the characteristic frequency f_0 between KLT-3 and KLT-7, while these values are one order of magnitude smaller than those of PMN, which could be due to restrained motions of Li ions located in strong off-center positions.

It should be noted that T_{VF} in relaxors is different from the freezing temperature in a dipole or spin glass because of the much more complicated nature of the dipolar

TABLE II. Experimentally determined parameters in the Vogel-Fulcher law of KLT-3, KLT-10, and PMN.

Substance	f_0 (Hz)	E_a (eV)	T_{VF} (K)	
KLT-3	9.7×10^9	0.045	0.045	Present study
KLT-7	4.8×10^{10}	0.088	56.3	Present study
PMN	1.03×10^{12}	0.0407	291.5	Ref. 27

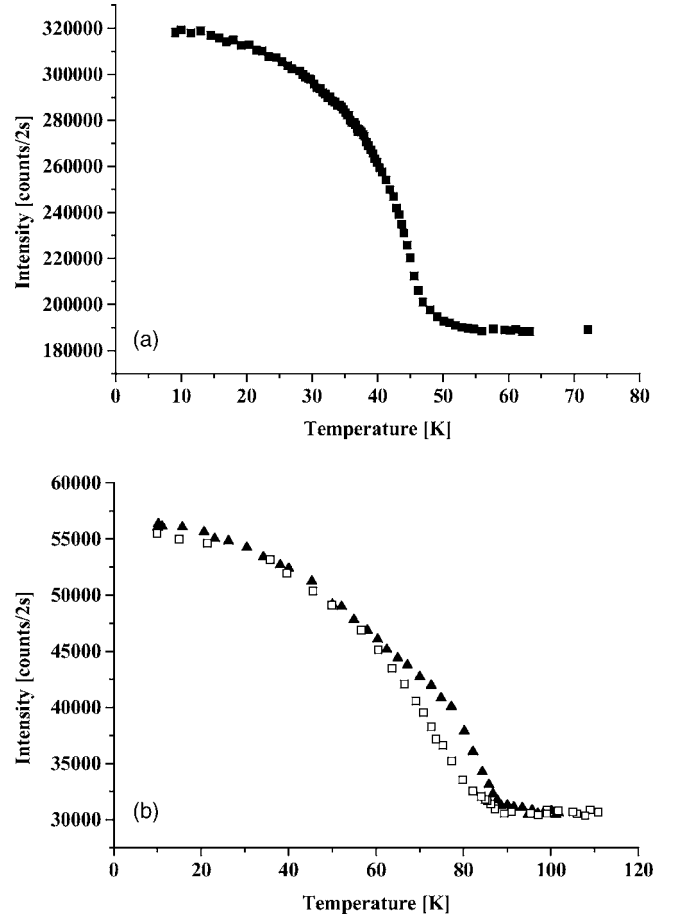


FIG. 10. Temperature dependences of (a) (220) neutron Bragg reflection intensities of KLT-3 and (b) (200) intensities of KLT-7.

relaxation.³⁰ In fact, the response of dipole moments of KLT-3 under the electric field exhibits a sudden slowing down at 40 K, which is higher than T_{VF} .¹⁸

E. Neutron-scattering experiments

Neutron elastic-scattering experiments are carried out on KLT-3 and KLT-7. Figures 10(a) and 10(b) show temperature dependences of (220) and (200) reflection intensities of KLT-3 and KLT-7, respectively. Both crystals exhibit steep increases of the intensities below T_p . This phenomenon can be attributed to the change of mosaicity of the crystal due to the appearance of ferroelectric microdomains which develop below T_p . The mosaicity of the crystal breaks the extinction law and makes the Bragg intensities increase.³¹ In KLT-7, a thermal hysteresis of about 7 K is observed, as shown in Fig. 10(b), which agrees with the SHG measurement.

IV. DISCUSSIONS

A. Pretransitional region between T_p and T_B

The most important finding of the present studies is the existence of a pretransitional state between the nonpolar cubic phase and the polar tetragonal phase. This can be disclosed mainly due to a combination study using a polarity-

sensitive SHG microscope and strain-sensitive x-ray diffraction on specimens cut from the same unpoled single crystal which was used in neutron-diffraction experiments. The temperature interval ΔT of the pretransitional region is determined to be 40 K in both KTL-3 and KTL-7, which agrees with the result of the neutron diffuse scatterings in KTL-6.⁷

The possible picture of the pretransitional region is as follows: In the cubic phase, dipole moments produced by off-centered Li ions align along one of the symmetry equivalent $\langle 100 \rangle$ directions. Below T_B , individual Li dipoles start to associate to form PNRs as a result of intracorrelations of Li dipoles. These correlations induce the deviation of the high-temperature behavior of dielectric constant and the appearance of diffuse scatterings. Upon further cooling down to T_p , PNRs interact with each other (intercorrelations) and develop with the size distribution. This is the origin of the characteristic frequency dispersion of dielectric responses. Because the polarization is local and the orientation is random above T_p , no SHG is observed. On the other hand, the lattice strains are induced by the average of polarization fluctuation $\langle (\Delta P)^2 \rangle$ through the electrostrictive effect. Lattice strains x_1 , x_3 and tetragonality t are expressed as

$$x_1 = Q_{13} \langle (\Delta P)^2 \rangle, \quad x_3 = Q_{33} \langle (\Delta P)^2 \rangle, \quad \text{and } t = x_3 - x_1 = (Q_{33} - Q_{31}) P_s^2. \quad (9)$$

This explains the quite small lattice anisotropies ($t=2 \times 10^{-4}$ for KLT-3 and 4×10^{-4} for KLT-7 in the vicinity of T_p) in the pretransitional region. Below T_p , the same expressions should hold with the same electrostrictive constants Q_{13} and Q_{33} but ΔP is replaced by the spontaneous polarization P_s . Since the magnitude of P_s is much larger than that of ΔP , larger strains and, consequently, larger tetragonality are induced, as shown in Fig. 6.

We would point out here that the structural phase transition at T_B from $Pm\bar{3}m$ to the nonpolar tetragonal phase, i.e., $P4/mmm$ with the long-range order, seems to be inconceivable because previous studies using infrared³² and hyper-Raman^{33,34} did not detect any change in phonon anomalies near T_B . We also performed neutron inelastic-scattering experiments using pure KTO, KLT-3, and KLT-7 and found that low-lying TO and TA phonons do not show any anomalies around T_B . This evidence supports that T_B is the Burns temperature and not a phase-transition temperature with long-range order.

B. Phase landscape in KLT

The phase below T_p is ferroelectric, even without the external electric field. It consists of ferroelectric microdomains which are supported by the neutron elastic-scattering experiments described in the previous section. The sizes of microdomains without an electric field are estimated to be less than the laser wavelength, as appreciable SHG cannot be observed without an electric field.

Based on these experimental results, the polarization states in three phases in KLT are illustrated, as shown in Fig.

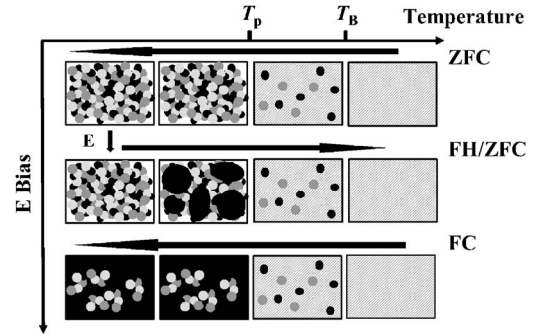


FIG. 11. Landscape of the polarization states in three phases in KLT. Gray region indicates nonpolar state and black and gray regions indicate polar state with different polarization orientations.

11. In the ZFC process, the high-temperature phase is nonpolar cubic $Pm\bar{3}m$ with uncorrelated individual shifts of Li and below T_B , PNRs appear in the cubic matrix. In the vicinity of T_B , the density of PNR is not large and each polar region fluctuates independently to form a superparaelectric state. The macroscopic symmetry of the intermediate phase is tetragonal as a result of the anisotropy of electrostrictive constants [Eq. (9)]. On approaching to T_p , PNRs start to interact with each other to increase the area with size distribution, which provides characteristic dielectric dispersion. Below T_p , a ferroelectric phase transition takes place accompanied by the microdomain state.

In the FC process, the polarization direction is easily aligned below T_p and a macroscopic polarization can be produced and maintained down to the low-temperature region. In the ZFC process, at a sufficiently low temperature, a random force originating from the random distribution of Li dipoles freezes a polar state, but the electric field cannot change the polarization direction. Thus, in the FH/ZFC process, a macroscopic polarization cannot be produced under the electric field up to a temperature near 40 K, where the thermal excitation overcomes the random force.

Finally, we would stress that KLT-3 and KLT-7 belong to a class of perovskite relaxors where the A sites are occupied by different kinds of isovalent atoms. Because almost all relaxors have a structure with B sites occupied by two kinds of heterovalent ions, KLT will be an important prototype relaxor for understanding the nature of relaxors.

ACKNOWLEDGMENTS

This work is supported by the Grants-in-Aid of Scientific Research (A) of MEXT, “Academic Frontier” Project of MEXT, and the 21st Century COE Program “Physics of systems with self-organization composed of multi-elements” of MEXT, Japan. We are grateful to Y. Yamada and Y. Tsunoda of the Waseda University, M. Maglione of the Institute of Condensed Matter Chemistry of Bordeaux, S. Vakhruchev of the Ioffe Physico-Technical Institute, Z.-G. Ye of the Simon Fraser University, and R. E. Cohen of the Carnegie Institution of Washington for their invaluable discussions.

- *Corresponding author. Electronic address: hiroko-9bq@uri.waseda.jp
- ¹U. T. Hochli, H. E. Weibel, and L. A. Boatner, *Phys. Rev. Lett.* **41**, 1410 (1978).
 - ²E. Courtens, *J. Phys. C* **14**, L37 (1981).
 - ³R. L. Prater, L. L. Chase, and L. A. Boatner, *Phys. Rev. B* **23**, 5904 (1981).
 - ⁴F. Borsa, U. T. Hochli, J. J. van der Klink, and D. Rytz, *Phys. Rev. Lett.* **45**, 1884 (1980).
 - ⁵S. R. Andrews, *J. Phys. C* **18**, 1357 (1985).
 - ⁶J. Toulouse, B. E. Vugmeister, and R. Pattnaik, *Phys. Rev. Lett.* **73**, 3467 (1994).
 - ⁷G. Yong, J. Toulouse, R. Erwin, S. M. Shapiro, and B. Hennion, *Phys. Rev. B* **62**, 14736 (2000).
 - ⁸H. Yokota, T. Oyama, and Y. Uesu, *Phys. Rev. B* **72**, 144103 (2005).
 - ⁹W. Kleemann and R. Lindner, *Ferroelectrics* **199**, 1 (1997).
 - ¹⁰K. Fujishiro, T. Iwase, Y. Uesu, Y. Yamada, B. Dkhil, J. M. Kiat, S. Mori, and N. Yamamoto, *J. Phys. Soc. Jpn.* **69**, 2331 (1982).
 - ¹¹J. J. van der Klink and D. Rytz, *J. Cryst. Growth* **56**, 673 (1982).
 - ¹²J. J. van der Klink, D. Rytz, F. Borsa, and U. T. Hochli, *Phys. Rev. B* **27**, 89 (1983).
 - ¹³Y. Uesu, S. Kurimura, and Y. Yamamoto, *Appl. Phys. Lett.* **66**, 2165 (1995).
 - ¹⁴Y. Uesu, R. Nakai, J. M. Kiat, C. Malibert, M. Itoh, and T. Kyomen, *J. Phys. Soc. Jpn.* **73**, 1139 (2004).
 - ¹⁵B. A. Strukov, E. L. Sorkin, N. K. Yushin, and S. A. Taraskin, *Fiz. Tverd. Tela (Leningrad)* **28**, 3171 (1986).
 - ¹⁶B. Salce, J. L. Graviil, and L. A. Boatner, *J. Phys.: Condens. Matter* **6**, 4077 (1994).
 - ¹⁷The spatial distribution of the effective electric field inside a specimen of KLT was calculated using the finite-element method of electrostatic field (PHOTO-VOLTBM, IT Assistcom). The result shows that the electric field is homogeneous and is directed to the [001] direction in the laser illuminated area.
 - ¹⁸H. Yokota and Y. Uesu, *J. Phys.: Condens. Matter* **19**, 102201 (2007).
 - ¹⁹E. A. Zhurova, V. E. Zavodnik, and V. G. Tsirel'son, *Crystallogr. Rep.* **40**, 753 (1995).
 - ²⁰R. D. Shannon and C. T. Prewitt, *Acta Crystallogr., Sect. B: Struct. Crystallogr. Cryst. Chem.* **B25**, 925 (1969).
 - ²¹G. D. Boyd, H. Kasper, and J. H. Mcfee, *IEEE J. Quantum Electron.* **QE-7**, 563 (1971).
 - ²²J. Jerphagnon, *Phys. Rev. B* **2**, 1091 (1970).
 - ²³A. F. Devonshire, *Philos. Mag.* **40**, 1040 (1949).
 - ²⁴Concerning the sign of the square root in Eq. (7), a confusion is found in texts and papers. The sign should be positive when the stability condition is duly considered.
 - ²⁵M. D. Agrawal and K. V. Rao, *J. Phys. C* **3**, 1120 (1970).
 - ²⁶U. T. Hochli, *Phys. Rev. Lett.* **48**, 1494 (1982).
 - ²⁷F. Wickenhofer, W. Kleemann, and D. Rytz, *Ferroelectrics* **124**, 237 (1991).
 - ²⁸D. Viehland, S. J. Jang, L. E. Cross, and M. Wuttig, *J. Appl. Phys.* **68**, 2916 (1990).
 - ²⁹D. Viehland, S. J. Jang, L. E. Cross, and M. Wuttig, *Phys. Rev. B* **46**, 8003 (1992).
 - ³⁰A. A. Bokov and Z.-G. Ye, *J. Mater. Sci.* **41**, 31 (2006).
 - ³¹M. Maglione, U. T. Hochli, J. Joffrin, and K. Knorr, *J. Phys.: Condens. Matter* **1**, 1527 (1989).
 - ³²V. Zelezny, A. Pashkin, J. Petzelt, M. Savinov, V. Trepakov, and S. Kapphan, *Ferroelectrics* **302**, 195 (2004).
 - ³³P. DiAntonio, B. E. Vugmeister, J. Toulouse, and L. A. Boatner, *Phys. Rev. B* **47**, 5629 (1993).
 - ³⁴H. Vogt, *Ferroelectrics* **202**, 157 (1997).